3D Bidomain modeling of cardiac virtual electrode pacing

P. Colli Franzone [*] L. F. Pavarino [†] S. Scacchi [†]

August 16, 2012

Introduction. While implantable cardiac pacemakers and cardioverter defibrillators are among the most important medical innovations of the twentieth century, researchers are still debating the basic mechanisms of cardiac excitation triggered by a pacemaker. Previous simulation studies have investigated the relevance of cardiac *virtual electrode responses* to unipolar cathodal and anodal stimulations for explaining the make and break excitation mechanisms and the induction of fibrillation and defibrillation, see e.g. [5, Ch. 4.4] and [14]. For a survey about the relationship between the virtual electrode polarization response and the outcome of the defibrillation shock see e.g. [15]. Most of these studies have considered 2D Bidomain models or cylindrical domains that by symmetry reduce to the 2D case. The goal of this work is to revisit these excitation mechanisms with detailed 3D orthotropic Bidomain simulations with transmural fiber rotation and augmenting the LRd membrane model [6] with the so-called *funny* and the *electroporation* currents. The heart can be stimulated electrically with rectangular current pulses in four different ways: by turning on a pulse with negative amplitude (cathode make, CM) or a positive amplitude (anode make, AM), and by turning off a pulse with negative amplitude (cathode break, CB) or positive amplitude (anode break, AB). It is well known that only Bidomain models with unequal anisotropy ratios of the intra- and extracellular media are able to generate *virtual electrode polarization* regions, see [11, 13] and [5, Ch. 2.1], experimentally observed by optical mapping, see [12] and [5, Ch. 4.3]. After an anodal stimulus, the transmembrane potential distribution exhibits a virtual anode (VA), i.e. a hyperpolarized volume around the stimulating electrode having a dog-bone shape, and by two virtual cathodes (VCs), i.e. depolarized regions adjacent to the concave part of the hyperpolarized anodal dog-bone boundary. Conversely, after a cathodal stimulus, the polarity is reversed, i.e. the transmembrane potential pattern exhibits a central dog-bone shaped VC oriented across fibers and two adjacent VAs aligned along fibers.

Methods. *Bidomain model.* The evolution of the transmembrane potential $v(\mathbf{x},t)$, extracellular potential $u_e(\mathbf{x},t)$, extracardiac potential $u_b(\mathbf{x},t)$, gating variables $w(\mathbf{x},t)$ and ionic concentrations $c(\mathbf{x},t)$ is described by the macroscopic Bidomain model (see [9, 10] for a derivation from a cellular model and [5, 7]):

$$\begin{cases} c_m\partial_t v - \operatorname{div}(D_i\nabla(v+u_e)) + i_{ion}(v,w,c) = 0 \text{ in } H \\ \partial_t w - R(v,w) = 0, \quad \partial_t c - S(v,w,c) = 0 \text{ in } H, \\ -\operatorname{div}(D_i+D_e)\nabla u_e = \operatorname{div} D_i\nabla v + i^e_{app}, \quad \text{in } H \\ -\operatorname{div}\sigma_b\nabla u_b = i^e_{app}, \quad \text{in } \Omega\setminus H, \\ \mathbf{n}^T D_i\nabla(v+u_e) = 0,\ \mathbf{n}^T D_e\nabla u_e = \mathbf{n}^T\sigma_b\nabla u_b \text{ on } \partial H, \\ u_e = u_b \text{ on } \partial H,\ \mathbf{n}^T\sigma_b\nabla u_b = 0 \text{ on } \partial\Omega \end{cases}$$

where $\overline{\Omega} = \overline{H}\cup\overline{\Omega}_0$ with H modeling a cardiac tissue in contact with a conducting medium Ω_0, representing either the intracavitary blood or an extracardiac bath. Here c_m and i_{ion} denote the capacitance and the ionic current of the membrane per unit volume, i^e_{app} represents the extracellular applied current per unit volume with the compatibility condition $\int_\Omega i^e_{app} = 0$, and σ_b is the conductivity coefficient of the extracardiac medium. In order to identify a unique solution of the Bidomain model, initial conditions on $v(\mathbf{x},0)$, $w(\mathbf{x},0)$, $c(\mathbf{x},0)$ must be added and a reference potential is chosen so that $\int_H u_e(\mathbf{x},t)dx = 0$.

Orthotropic fiber structure. Beside the intramural fiber structure across the ventricular wall, recent studies have evidenced a laminar organization of the fibers, yielding two preferential transverse fiber directions, one tangent and the other orthogonal to the laminae, respectively. This geometrical fiber architecture yields orthotropic properties of the effec-

[*]Dipartimento di Matematica, Università di Pavia, Via Ferrata 1, 27100 Pavia, Italy. E-mail: colli@imati.cnr.it.

[†]Dipartimento di Matematica, Università di Milano, Via Saldini 50, 20133 Milano, Italy. E-mail: luca.pavarino@unimi.it, simone.scacchi@unimi.it.

tive macroscopic conductivity tensors, see [8]. The orthotropic macroscopic conductivity tensors $D_i = D_i(\mathbf{x})$ and $D_e = D_e(\mathbf{x})$ at any point $\mathbf{x} \in H$ are defined by:

$$D_{i,e} = \sigma_l^{i,e}\ \mathbf{a}_l\mathbf{a}_l^T + \sigma_t^{i,e}\ \mathbf{a}_t\mathbf{a}_t^T + \sigma_n^{i,e}\ \mathbf{a}_n\mathbf{a}_n^T,$$

where $\mathbf{a}_l = \mathbf{a}_l(\mathbf{x})$ is a unit vector parallel to local fiber direction and $\mathbf{a}_t = \mathbf{a}_t(\mathbf{x})$, $\mathbf{a}_n = \mathbf{a}_n(\mathbf{x})$ are unit vectors tangent and normal to the local fiber lamina, respectively. Moreover, $\sigma_{l,t,n}^{i,e}$ denote the effective intra and extracellular conductivity coefficients measured along and across the fiber direction tangent and normal to the fiber lamina, whose values are given by $\sigma_l^i = 2.3172$, $\sigma_t^i = 0.2435$, $\sigma_n^i = 0.0569$ and $\sigma_l^e = 1.5448$, $\sigma_t^e = 1.0438$, $\sigma_n^e = 0.37222$, all in $mScm^{-1}$; for the calibration of these values see [2]. The transmural fibers rotate linearly across the thickness, counterclockwise from epicardium (-75^o) to endocardium (45^o), for a total amount of 120^o. We also incorporate the epi-endocardial obliqueness of the fibers by introducing the so called *imbrication angle* which describes the deviation of $\mathbf{a_l}$ from the tangent plane of the packed ellipsoidal surfaces, see for details [3].

Membrane model. We choose the LRd ionic model [6], augmented with the addition of i) the funny current I_f; ii) the electroporation current I_e; iii) the outward current I_a activated upon induced depolarization. This membrane model exhibits an action potential duration of about 210 ms. For further details about the calibration of these currents see [2].

Numerical methods. The cardiac domain H considered is a block of a truncated ellipsoidal volume modeling a portion of the left ventricular wall. The endocardial surface is in contact with an ellipsoidal volume modeling the blood cavity with conductivity $\sigma_b = 6\ mScm^{-1}$. In all computations, a structured grid of hexahedral isoparametric Q_1 finite elements of size of about $h = 0.1\ mm$ is used in space, while the time discretization is performed by a double operator splitting procedure, based on splitting both the ODEs from the PDEs and the elliptic PDEs from the parabolic one, see for details [1, 16]. The parallel Fortran code used in the simulations is based on the PETSc library *http://www.mcs.anl.gov/petsc* and it is run on 24 processors of a Linux Cluster with 56 Opteron AMD processors and Infiniband network.

Results. *S1 stimulation.* We first apply at a small volume centered on the epicardial surface of the resting tissue an initial S1 cathodal ($i_{app}^e < 0$) stimulus initiating a propagating excitation wavefront that

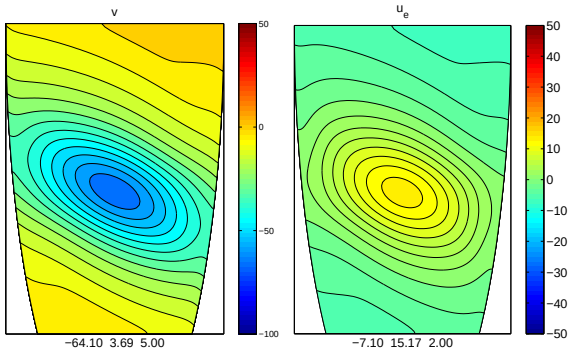

Figure 1: Epicardial transmembrane (left) and extracellular (right) potential distributions 200 ms after the S1 stimulus, i.e. at the instant when the S2 stimulation starts.

sweeps the cardiac domain. In order to ensure the compatibility condition, we inject an equal total stimulation current of opposite polarity in a thin strip of the extracardiac bath. The epicardial transmembrane and extracellular potential distributions 200 ms after the S1 stimulus, i.e. during the relative refractory period (RRP), are reported in Fig. 1. At this instant a premature S2 cathodal ($i_{app}^e < 0$) stimulus of duration 10 ms is delivered at the same subepicardial thin volume of the S1 pulse. We investigate the excitation patterns elicited applying a premature stimulus of threshold strength, i.e. no excitation response is elicited below this strength value, and above threshold strength.

S2 threshold stimulation. Fig. 2 reports the epicardial transmembrane and extracellular potential distributions generated by a cathode break excitation mechanism, at three time instants after the onset of a threshold S2 stimulus of strength $-0.0243\ mA$ and 10 ms duration delivered 200 ms after the S1 stimulus. During the stimulation, the tissue under the cathode is strongly depolarized and at the end of the $S2$ stimulus pulse the transmembrane potential reaches a maximum value of about 118 mV. The transmembrane potential exhibits a cathodal region around the site of stimulation (virtual cathode) with a pair of hyperpolarized regions (virtual anodes) developing along fibers. Because the $S2$ stimulus is still applied during the RRP, the depolarized tissue under the cathode is not excitable, thus cathode make excitation does not occur. After the stimulus end, the hyperpolarized tissue around the virtual anodes

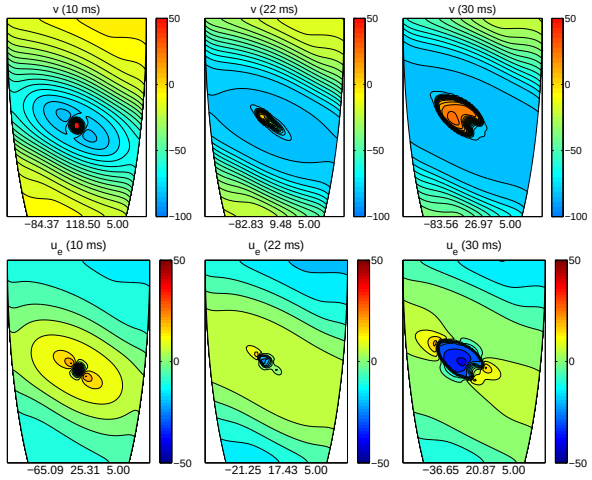

Figure 2: Cathode break excitation mechanism, threshold stimulus. Epicardial transmembrane (top row) and extracellular (bottom row) potential distributions at three time instants after an S2 stimulus of strength $-0.0243\ mA$ and 10 ms duration delivered 200 ms after the S1 stimulus.

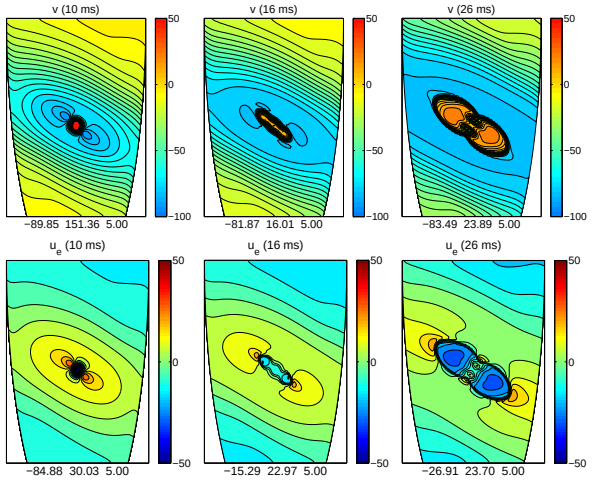

Figure 3: Cathode break excitation mechanism, far above threshold stimulus. Epicardial transmembrane (top row) and extracellular (bottom row) potential distributions at three time instants after an S2 stimulus of strength $-0.0432\ mA$ and 10 ms duration delivered 200 ms after the S1 stimulus.

removes the inactivation of the sodium channels, rendering the tissue excitable. In a slab tissue of rotating fibers on parallel planes, it is expected that the electrotonic currents (charge diffusion), flowing from the virtual cathode towards the virtual anodes, are able to originate simultaneously two activation wavefronts. In this case instead, due to the combined effect of fiber rotation, imbrication angle and tapering of the ventricular thickness, the excitation wavefront starts only from one of the two virtual anodes at about 10 ms after the end of the S2 stimulus. The excitation wavefront is initially an open broken surface with the rim lying on the border of the virtual cathode. The extracellular potential presents at 10 ms two maxima of almost equal magnitude in the virtual anodes and a minimum inside the virtual cathode. At 22 ms a more pronounced positive maximum, located in one of the virtual anodes ahead of the negative area, indicates that an excitation wavefront starts to propagate along the fiber direction. At 30 ms, some extracellular potential maxima appears ahead of the portions of the excitation wavefronts propagating mainly along the fiber direction.

S2 above-threshold stimulation. Fig. 3 reports the epicardial transmembrane and extracellular potential distributions generated by a cathode break excitation mechanism, at three time instants after the onset of a far above-threshold S2 stimulus of strength $-0.0432\ mA$ and 10 ms duration delivered 200 ms after the S1 stimulus. In this case, the electrotonic currents flowing from the virtual cathode to the virtual anodes are strong enough to excite both the virtual anodes, hence two activation wavefronts start to propagate and subsequently merge. The extracellular patters exhibit two symmetric maxima of comparable magnitude ahead of the portions of the excitation wavefronts propagating mainly along fiber.

Conclusion. We have simulated cathode break excitation mechanisms in a 3D orthotropic Bidomain model. As already shown in [5, Ch. 4.3] by 2D Bidomain simulations, cathode break excitation following strong S2 cathodal pulses is able to generate quaterfoil reentry phenomena. Our results have shown that low voltage cathodal stimulations near threshold induce broken asymmetric activation wavefronts, that might constitute a dangerous arrhythmogenic substrate, e.g. for fronts associated to reduced action potential durations and slow conduction velocities, possibly leading to reentrant pathways with an excitable gap. Finally, we observe that a similar transition from an asymmetric to a symmetric wavefront propagation depending on the stimulation

strength occurs also in diastole for anode make excitation mechanisms.

Limitations. Our study has focused on S2 stimulations delivered in the same site of the first S1 pulse at an instant within the systolic phase. A further extension would be to compute the strength-interval curve, as we have done in [2] for a three-dimensional slab, investigating more deeply the temporal window where the asymmetric excitation occurs.

We have considered an idealized ventricular geometry consisting only of a portion of truncated ellipsoid. It would be interesting to extend this study to more realistic geometries and pre-shock substrates, as e.g. in [4].

References

[1] Colli Franzone P., Pavarino L.F. and Scacchi S. Exploring anodal and cathodal make and break cardiac excitation mechanisms in a 3D anisotropic bidomain model. *Math. Biosci*, 230: 96–114, 2011.

[2] Colli Franzone P., Pavarino L.F. and Scacchi S. Cardiac excitation mechanisms, wavefront dynamics and strength-interval curves predicted by 3D orthotropic bidomain simulations *Math. Biosci*, 235: 66–84, 2012.

[3] Colli Franzone P., Guerri L., Pennacchio M. Spreading of Excitation in 3-D Models of the Anisotropic Cardiac Tissue. II. Effect of Geometry and Fiber Architecture of the ventricular wall. *Math. Biosci.*, 147: 131-171, 1998.

[4] Constantino J., Long Y., Ashihara T. and Trayanova N.A. Tunnel propagation following defibrillation with ICD shocks: hidden postshock activations in the left ventricular wall underlie isoelectric window. *Heart Rhythm*, 7: 953–961, 2010.

[5] Efimov I.R., Kroll M.W. and Tchou P.J. (Eds), *Cardiac Bioelectric Therapy* , Springer Science+Business Media, LLc, 2009.

[6] Gima K. and Rudy Y. Ionic current basis of electrocardiographic waveforms. A model study. *Circ. Res.*, 90: 889–896, 2002.

[7] Henriquez C. S. Simulating the electrical behavior of cardiac tissue using the bidomain model. *Crit. Rev. Biomed. Eng.*, 21: 1–77, 1993.

[8] Hooks D.A. et al. Laminar arrangement of ventricular myocytes influences electrical behavior of the heart. *Circ. Res.*, 101: e103–e112, 2007.

[9] Neu J.S. and Krassowska W. Homogenization of Syncitial Tissues. *Crit. Rev. Biom. Engr.*, 21 (2): 137–199, 1993.

[10] Pennacchio M., Savarè G. and Colli Franzone P. Multiscale modeling for the bioelectric activity of the heart. *SIAM J. Math. Anal.*, 37 (4): 1333–1370, 2006.

[11] Roth B.J. A mathematical model of make and break electrical stimulation of cardiac tissue by a unipolar anode or cathode. *IEEE Trans. Biomed. Eng.*, 42: 1174–1184, 1995.

[12] Sidorov V.Y. et al. Examination of stimulation mechanism and strength-interval curve in cardiac tissue. *Am. J. Physiol Heart Circ. Physiol.*, 289: H2602–H2615, 2005.

[13] Skouibine K.B., Trayanova N.A. and Moore P. Anode/cathode make and break phenomena in a model of defibrillation. *IEEE Trans. Biomed. Eng.*, 46 (7): 769–777, 1999.

[14] Trayanova N.A. Defibrillation of the heart: insights into mechanisms from modelling studies. *Exp. Physiol.*, 91 (2): 323–337, 2006.

[15] Trayanova N.A., G. Plank and B. Rodriguez. What have we learned from mathematical models of the defibrillation and postshock arrhythmogenesis? Application of bidomain simulations. *Heart Rhythm*, 3 (10): 1232–1235, 2006.

[16] Vigmond E.J. et al. Solvers for the cardiac bidomain equations. *Progr. Biophys. Molec. Biol.*, 96: 3–18, 2008.